



# Electrochemical characterization and post-mortem analysis of aged LiMn<sub>2</sub>O<sub>4</sub>–Li(Ni<sub>0.5</sub>Mn<sub>0.3</sub>Co<sub>0.2</sub>)O<sub>2</sub>/graphite lithium ion batteries. Part I: Cycle aging

Barbara Stiaszny <sup>a</sup>, Jörg C. Ziegler <sup>a,\*</sup>, Elke E. Krauß <sup>a</sup>, Jan P. Schmidt <sup>b</sup>, Ellen Ivers-Tiffée <sup>b</sup>

<sup>a</sup> Robert Bosch GmbH, Corporate Sector Research and Advance Engineering, Postfach 10 60 50, 70049 Stuttgart, Germany

<sup>b</sup> Institut für Werkstoffe der Elektrotechnik (IWE), Karlsruher Institut für Technologie (KIT), Adenauerring 20b, 76131 Karlsruhe, Germany



## HIGHLIGHTS

- Comprehensive analysis of new and cycle aged cells by numerous methods.
- Application of the DRT to impedance spectra.
- Aged anodes show a reduced overall impedance.
- Dominant aging mechanisms have been clarified.

## ARTICLE INFO

### Article history:

Received 4 July 2013

Received in revised form

4 November 2013

Accepted 22 November 2013

Available online 3 December 2013

### Keywords:

Aging mechanisms

Cycle aging

LiMn<sub>2</sub>O<sub>4</sub>

NMC

Lithium ion battery

Impedance spectroscopy

## ABSTRACT

A detailed capacity fade analysis was carried out for a commercial lithium ion battery with a mixed LiMn<sub>2</sub>O<sub>4</sub>/NMC cathode, cycled at room temperature with a continuous discharge rate of 1C. Complementary electrochemical and physical-analytical investigations revealed that the most significant aging processes was loss of cycleable lithium due to SEI-layer formation on the anode. The layer formation is accelerated by transition metals coming from the cathode. Impedance spectroscopy proved a significant increase of the cathode charge transfer resistance and of the serial resistance due to electrolyte decomposition and the formation of a surface layer on the anode.

The changing of the impedance spectra of the lithium ion battery with aging could be interpreted with the help of impedance spectra of symmetric cells. From DRT analysis equivalent circuits for anode and cathode were derived, which were used for fitting of the impedance spectra.

© 2013 Elsevier B.V. All rights reserved.

## 1. Introduction

The high power and energy density of lithium ion batteries have made them one of the most attractive energy storage systems. Nowadays they are widely used in portable electronic devices like laptops, cameras and mobile phones. In the past few years lithium ion batteries have drawn much attention for their operation in automotive applications like hybrid vehicles (HEV), plug-in hybrid electric vehicles (PHEV) and full electric vehicles (EV). These applications require long cycle and calendar life typically up to 15 years, low cost, high power and safe operation.

Although there is a large variety of possible materials combination for electrodes in lithium ion batteries, combining high cycle stability and high specific capacity reduces the choices to a handful. Promising candidates for cathodes are layered oxides like Li(Ni<sub>1/3</sub>Co<sub>1/3</sub>Mn<sub>1/3</sub>)O<sub>2</sub> which exhibits high specific capacity [1], but discharge at high rates is limited. To increase safety and especially rate capability in the cell, LiMn<sub>2</sub>O<sub>4</sub> is added to the cathode because it exhibits the fast kinetics that is necessary for high power applications [1] while at the same reducing the battery's cost. On the other hand, Mn-rich compounds are preferred compared to Ni- or Co-rich materials, although their specific capacity is lower and LiMn<sub>2</sub>O<sub>4</sub> suffers from manganese dissolution [2]. The best anode material considering both specific capacity and cycleability is graphite [2].

\* Corresponding author. Tel.: +49 711 811 7626; fax: +49 711 811 5119333.

E-mail address: [joerg.ziegler@de.bosch.com](mailto:joerg.ziegler@de.bosch.com) (J.C. Ziegler).

It is commonly known that life time of lithium ion batteries is limited by unwanted side reactions [3]. These side reactions may affect all parts of a battery including the electrolyte, the active material, binder, conducting agents, current collectors and the separator which results in capacity decrease and/or increase of the overall cell impedance [3–5].

Understanding the substantial aging mechanisms in lithium ion batteries is of great importance to face life time challenges and to make correct life time predictions. In this work aging phenomena are investigated by several analytical methods as well as electrochemical impedance spectroscopy.

## 2. Experimental

### 2.1. Cell type

Commercial 18650 lithium ion batteries containing a blend of  $\text{LiMn}_2\text{O}_4$  and  $\text{Li}(\text{Ni}_{0.5}\text{Mn}_{0.3}\text{Co}_{0.2})\text{O}_2$  as cathode material and graphite as anode material with an initial capacity of 2 Ah have been used in this work.

### 2.2. Cell cycling

Before cycle aging the cells were characterized by a power and capacity test. In order to determine the power and inner resistance 12 A discharge pulses were applied for 10 s at different SOCs (between SOC100 and SOC10 in steps of 10% SOC). The voltage and current were taken just prior to the pulse and at the end of the pulse after 10 s to calculate the inner resistance by the following equation (1).

$$R_{DC} = \frac{U_{10\text{ s}} - U_{0\text{ s}}}{I_{10\text{ s}} - I_{0\text{ s}}} = \frac{\Delta U}{\Delta I} \quad (1)$$

The specific power in  $\text{W kg}^{-1}$  was calculated by multiplication of voltage and current at the end of the pulse after 10 s divided by the mass of the cell as shown in equation (2).

$$P = \frac{U_{10\text{ s}} \cdot I_{10\text{ s}}}{m_{\text{Cell}}} \quad (2)$$

The capacity was determined at a discharge rate of 1C and C/5 to a voltage of 2.75 V.

After the power and capacity test, the standard charging procedure recommended by the manufacturer was applied. Cells were charged at a constant current rate of 1 A from 2.75 V to 4.2 V and subsequently the potential was held constant at 4.2 V until the total charging time exceeded 3 h.

Six identical cells were cycled 800 times at room temperature using a continuous discharge rate of 2 A and the standard charging procedure as described above. During cycling the power and the C/5 capacity was monitored every 100 cycles. The cycling and the characterization were carried out with a BaSyTec Battery Cycler.

### 2.3. Laboratory test cells

For post mortem analysis and characterization of the uncycled cell, the batteries were opened in an argon-filled glovebox. Electrode disks with a diameter of 18 mm were punched out of the cell roll for use in EL-Cells, which are commercially available test cells [6]. Before using the electrode sheets the coating had to be removed on one side of the current collector in order to get electrical contact. Particularly with aged electrodes the coating easily flakes off or sticks to the separator, making it a challenge to gain fully coated electrode sheets. After removing the coating the sheet was washed

in dimethyl carbonate and dried at room temperature to remove residuals from the electrolyte of the cell.

In total three types of test cells were prepared.

- *Half cells* having anode or cathode as working electrode and metallic lithium as counter and reference electrode (e.g. data shown in Figs. 8 and 9).
- *Full cells* with cathode and anode plus metallic lithium as reference electrode to monitor the potentials of anode and cathode during cycling (e.g. data shown in Fig. 10).
- *Symmetric cells* with two cathodes or two anodes [7] (e.g. data shown in Figs. 3, 13 and 14).

In order to prepare symmetric cells at an arbitrary SOC, two identical laboratory test cells had to be assembled and charged to the desired SOC beforehand. These cells were cycled at low rate for 3 cycles and set at the same desired voltage. Afterwards the cells were disassembled in the glovebox, and the electrodes were washed and dried and directly placed into the symmetric arrangement. The procedure of rearranging already assembled cells is problematic, because the coating easily flakes off and surface layers are always affected during contact with dry atmosphere. This makes it nearly impossible to investigate surface layers or contact resistances between the active material and the current collector.

We differentiate between new and aged symmetric cells. For new symmetric cells two identical full cells with reference electrodes were built and the voltage was set by a discharge with a determined discharge capacity. This allowed for the cell to be set to a certain SOC related to its initial full cell capacity. After discharge the two cathodes and the two anodes were incorporated into symmetric cells. In contrast, for aged symmetric cells two identical half cells with reference electrodes were constructed and set to a desired voltage by a voltage limiting discharge step. A discharge step with a determined discharge capacity would lead to a different voltage compared to the new state, due to a reduced capacity in the aged state. Afterwards with both electrodes a symmetric cell was built.

A glass fibre separator with a diameter of 18 mm and a thickness of 1.55 mm served as the electrolyte reservoir. 1 M  $\text{LiPF}_6$  in a mixture of ethylene carbonate (EC) and dimethyl carbonate (DMC) at a ratio of 1:1 (v/v%) was used as the electrolyte in the laboratory test cells.

### 2.4. Electrochemical investigation

A slow constant current discharge at C/50 was conducted at the aged electrode to distinguish between capacity losses from active material degradation and an increase in inner resistance. Slow-scan cyclic voltammetry was carried out at anode and cathode half cells at a scanning rate of  $5 \mu\text{V s}^{-1}$  to investigate the redox voltages and peak heights of new and aged electrodes.

Furthermore half cells and full cells were subjected to rate tests with C-Rates between C/10 and 5C to check the rate capability of new and aged electrodes.

Full cells with reference electrodes were assembled to measure the potentials of the anode and cathode during cycling of new and aged cells. In these experiments the potentials of anode and cathode were monitored against the reference electrode while cycling the cell between 4.2 V and 2.75 V.

Electrochemical impedance spectroscopy was carried out using a Gamry Instruments Potentiostat PCI4G300-51021 (Series-G300). Full batteries were discharged at a rate of C/5 and kept at OCV for four hours before the measurement started. The impedance of batteries was measured in hybrid mode every 100 cycles in the frequency range between  $10^5 \text{ Hz}$  and  $2 \text{ mHz}$  with a

perturbation voltage of 1 mV at temperatures of 23 °C, 0 °C and –10 °C. Test cells were directly investigated after assembly between 3·10<sup>5</sup> Hz and 2 mHz at the same perturbation voltage and at temperatures of 23 °C, 10 °C and 0 °C. Before the measurement the battery was kept for three hours at the desired temperature to be equilibrated. Temperature control was achieved in a climate chamber.

## 2.5. Physical-analytical investigation

Electrode sheets were washed in dimethyl carbonate and dried at room temperature before each investigation. XRD measurements were conducted with a Bruker D8 Advance with a wavelength of CuK $\alpha_1$  = 1.5405 Å covering the diffraction-angle range 5 < Θ < 85. Surface investigations were done by a Gemini Leo 1530 scanning electron microscope equipped with Oxford Instruments analytical tools. For surface pictures typically an acceleration voltage of 5 kV was used, whereas for EDS analysis 20 kV was selected. Micro-sections investigated with a Zeiss Axioplan light microscope were used to determine layer thicknesses.

Concentrations of transition metals at the anode were ascertained by ICP-OES measurements, where the sample was dissolved in nitrohydrochloric acid. The electrolyte of the battery was leached out by methylene chloride after disassembling so that non-volatile constituents could be determined by GC-MS.

As a reference state, a pristine cell was fully characterized by the designated methods, which is labelled as a “new cell” in the following text and graphs.

## 2.6. Analysis of electrochemical impedance spectra by the distribution of relaxation times (DRT)

Within impedance spectra processes are often overlapping and cannot be separated in the Nyquist plot. An improved separation of processes can be achieved by calculating the distribution function of relaxation times (DRT). This method was originally developed to evaluate impedance spectra of solid oxide fuel cells by the Institut für Werkstoffe der Elektrotechnik at the Karlsruher Institute of Technology and was presented in detail in Refs. [8–10]. Considering the simplest case of an ideal polarization process it can be described by a parallel connection of an ohmic resistance  $R$  and a capacitance  $C$  in an equivalent circuit. The corresponding time constant of this circuit can be written as

$$\tau_{RC} = RC = \frac{1}{2\pi f}. \quad (3)$$

For a mathematically description the Distribution Function of Relaxation Times  $g(\tau)$  replaces the single  $RC$  element. The upper schematic in Fig. 1 shows an example of  $g(\tau)$  for two serial

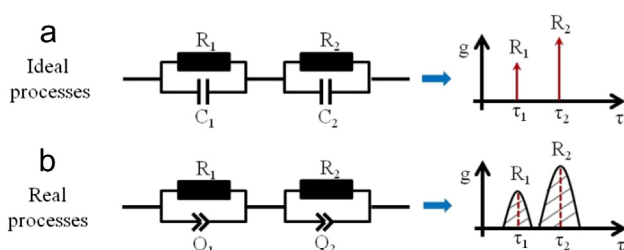


**Fig. 1.** DRT for a) ideal processes described by  $RC$  parallel combinations, b) real processes described by  $RQ$  parallel combinations.

connected  $RC$  elements having two discrete time constants. Polarization processes in real systems, like in battery electrodes with a complex microstructure, are characterized by a distribution of time constants around a main relaxation time as shown in the lower part of Fig. 1. Integration of the peak area gives the resistance of the corresponding  $RQ$ -element.

The relation between the impedance and a single  $RC$ -circuit element is given by equation (4) and can be written as

$$Z_{RC}(\omega) = \frac{R}{1 + i\omega RC} = \frac{R}{1 + i\omega\tau} \quad (4)$$

Equation 4 can be extended by the introduction of the distribution function of relaxation times  $g(\tau)$  using an infinite number of  $RC$ -elements with various time constants reaching from 0 to  $\infty$ , which is expressed as [8]

$$Z_{pol}(\omega) = \int_0^{\infty} \frac{g(\tau)}{1 + i\omega\tau} d\tau. \quad (5)$$

Thus the relation between the total impedance and its DRT is given by Ref. [8]

$$Z(\omega) = R_0 + Z_{pol}(\omega) = R_0 + R_{pol} \cdot \int_0^{\infty} \frac{g(\tau)}{1 + i\omega\tau} d\tau \quad (6)$$

where  $R_0$  is the ohmic resistance and  $R_{pol}$  the overall polarization. By means of the calculated DRTs, a separation of the loss processes can be conducted and an adequate electrical equivalent circuit can be derived to fit the impedance spectra.

## 3. Results and discussion

### 3.1. Investigation of the new cell by impedance spectroscopy

Two cells were characterized in parallel by electrochemical impedance spectroscopy following a matrix of 11 SOCs each measured at three different temperatures (0, 10, 23 °C). Temperature variation can help to separate the occurring processes in the electrochemical cell, which has already recently been demonstrated by Refs. [11,12]. Electrochemical processes in the cell appear as a phase shift in the Bode plot of the impedance spectrum, which are here denominated as P1 and P2. Fig. 2 shows the measured spectra for 11 SOCs at 0 °C in Nyquist and Bode plot.

Considering the Bode plot in Fig. 2b it can be seen that the dominant process between 10<sup>0</sup> and 10<sup>-1</sup> Hz, indicated as P1, drastically increases with decreasing state of charge, especially between SOC0 and SOC20. Also the total impedance decreases with increasing state of charge between SOC0 and SOC40. Between SOC40 and SOC90 no significant change in the total impedance can be observed, while the total impedance of SOC100 is similar to SOC30, which means an inversion in the aforementioned trend. The SOC dependency of P2 is not as strong as for P1. Also P2 is already influenced by the inductive behaviour of the 18650 cell for high frequencies, due to the windings of the electrode sheets. The intersection of the impedance curve the x-axis of the Nyquist plot, corresponding to the sum of all ohmic contributions in the cell, does not show an SOC dependency.

To be able to fully separate P1 and P2 and to assign them to anode or cathode, impedance measurements on symmetric anode and cathode cells were performed at various SOCs and temperatures. Fig. 3 shows impedance spectra of 6 symmetric cathode and anode cells at 0 °C in Nyquist and Bode plots. It was necessary to prepare 6 similar cells with different SOCs, because

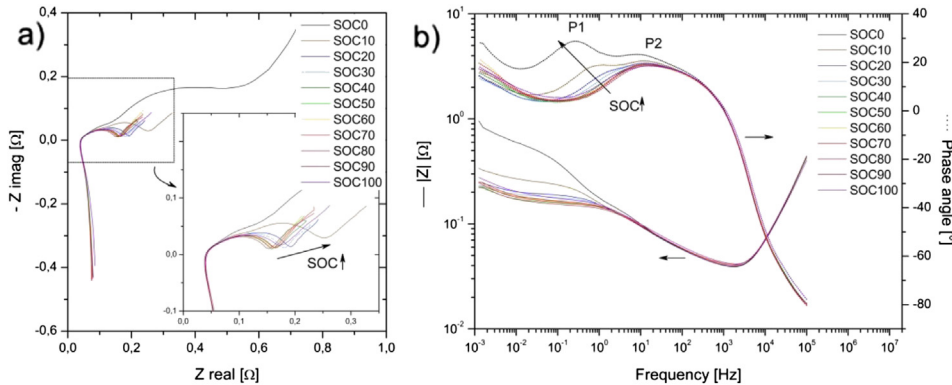


**Fig. 2.** Impedance spectra of the 18650 battery at various SOCs and 0 °C in a) Nyquist and b) Bode plots. The solid line in Fig. 2b represents the impedance, the dashed line represents the phase angle. Occurring processes are marked as P1 and P2. The impedance increases with decreasing SOC.

the potential of the electrodes cannot be varied within symmetric cells.

Comparing the frequency of processes in symmetric cells and full batteries allows the assignment of P1 to the cathode and P2 to the anode both representing the charge-transfer processes [13,14]. Fig. 2 marks the frequency domains of symmetric cells in the 18650 full cell spectra. The impedance spectra of the symmetric cells show the same trend in SOC-dependence as seen for

the complete cell in Fig. 2. It can also be seen, that another small process P3K and P3A occurs in the high frequency domain (10<sup>4</sup>–10<sup>5</sup> Hz) of both spectra, which was hidden by the inductive tail in the full battery's spectra. This small process originates from contacts between particles or between particles and the current collector [15]. The variations in the high-frequency processes in Fig. 3b and d can be attributed to sample preparation, which applies mechanical stress to the electrode, when the coating was

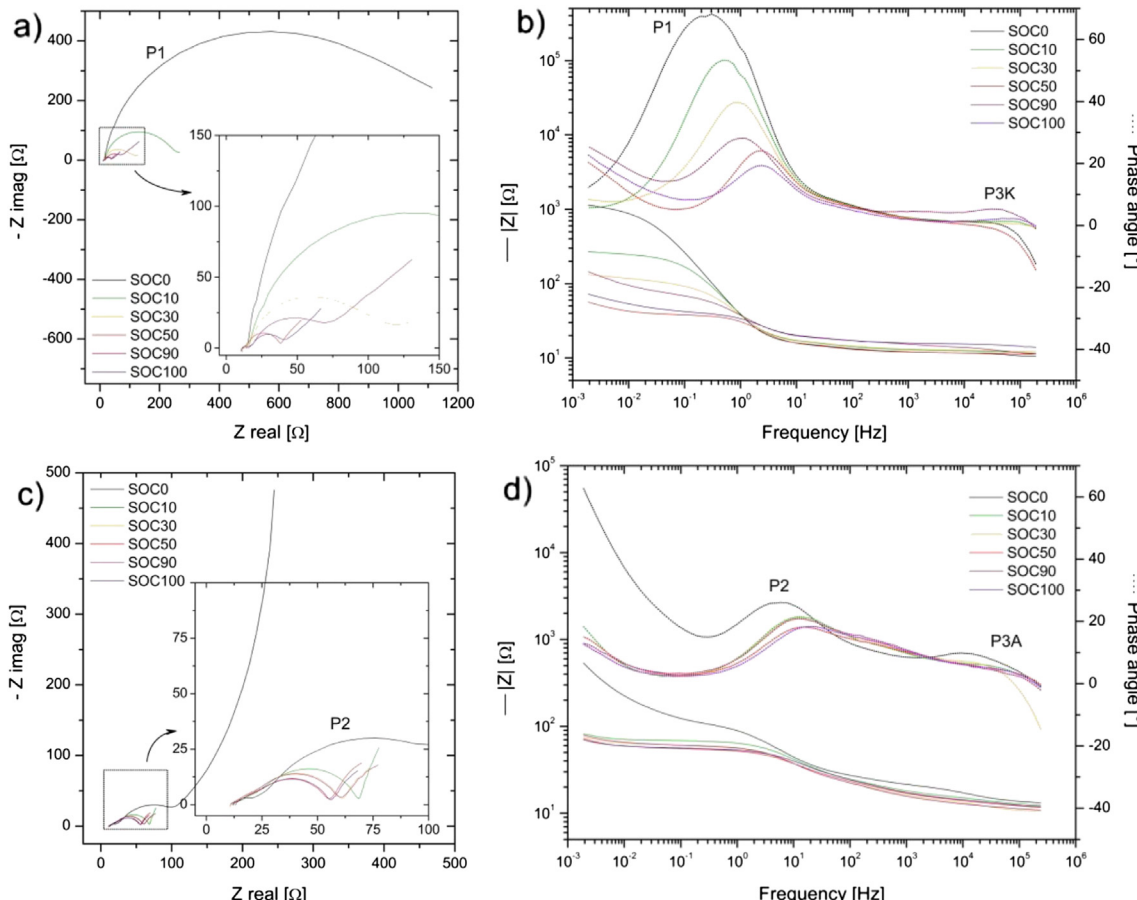


**Fig. 3.** Impedance spectra of a + b) symmetric cathode and c + d) symmetric anode cells at various SOCs at 0 °C in Nyquist and Bode plots. Occurring processes are marked as P1, P2, P3K and P3A. Occurring processes in Fig. 2 can now be attributed to either the anode or the cathode.

removed from one side of the double-sided electrode sheets. Small inductive tails may occur for both electrodes in Fig. 3 deriving from the measurement cables.

### 3.2. Materials analysis of the new cell

Materialographic specimens were cross-sectioned and polished to obtain information about the microstructure and the thickness of the electrodes. The cathode in its new state has an average electrode thickness of 77 µm, the aluminium current collector 22 µm, while the anode's average thickness is 58 µm and the copper current collector 9 µm.

EDX analysis proved the composition of spinel and NMC particles. Small amounts of magnesium are added to the spinel structure, which is well known to stabilize it during cycling by a reduced Jahn-Teller distortion [2,16]. From the EDX-analysis it can also be seen that the NMC has a Ni:Co:Mn composition of 5:3:2, i.e. LiNi<sub>0.3</sub>Mn<sub>0.3</sub>Co<sub>0.2</sub>O<sub>2</sub>.

X-ray diffraction analysis was carried out for the cathode between SOC0 and 100 to see how the lattice parameter and lattice volume changes during charging. Fig. 4a shows the change in the cubic lattice constant  $a$  of LiMn<sub>2</sub>O<sub>4</sub> in the blend cathode and Fig. 4b gives the variation of  $a$  and  $c$  parameter of hexagonal NMC.

The black curve in Fig. 4a, corresponding to LMO, shows no change in lattice parameter between SOC0 and 40, which is in accordance with results from Winter et al. [2] and to our results from cyclic voltammetry, where LMO does not show any activity below 3.8 V corresponding to about SOC40 in the cell. Opposite to that, NMC shows activity nearly over the whole working range. The layered NMC experiences a change of its two lattice constants in opposite directions. The  $a$ -parameter decreases when increasing

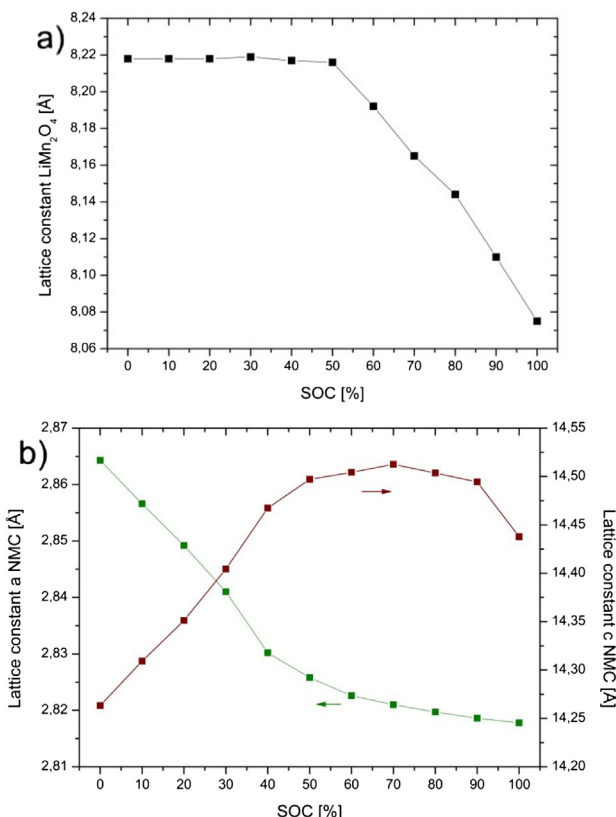


Fig. 4. a) Dependence of lattice constant  $a$  of LiMn<sub>2</sub>O<sub>4</sub> with change of SOC. b) Dependence of lattice constants  $a$  and  $c$  of NMC with change of SOC.

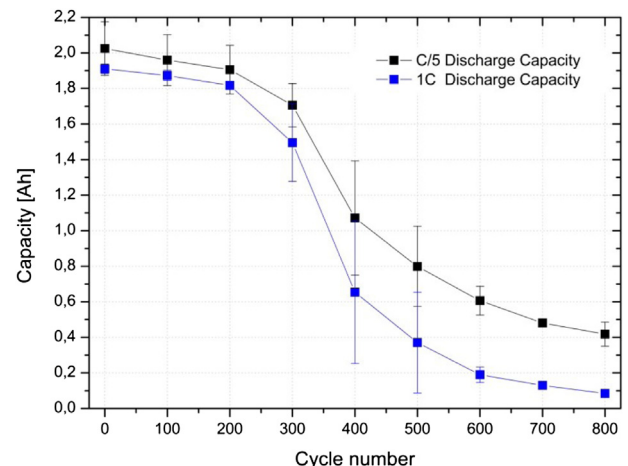


Fig. 5. Capacity decrease at 1C and C/5 discharge rate during cycle aging at room temperature (description of cycle aging see Experimental section). Error bars represent the standard deviation of six identical cells.

the state of charge, while the  $c$ -parameter increases. The total change in the lattice volume during charging is thus very small at about 1% between SOC0 and SOC100. Parameter  $c$  is sensitive for changes in interlayer distances, while parameter  $a$  indicates variations within a layer, which is in accordance to results from Nam et al. [17].

### 3.3. Investigation during cycling

During cycling the capacity of the six identical cells was monitored at a discharge rate of 1C and C/5 as shown in Fig. 5. It can be seen that the capacity decreases drastically within 800 cycles with a steep drop starting at about 200 cycles. Furthermore the devolution of power and inner resistance at 10 different SOCs (SOC100–SOC10) of one cell are plotted in Fig. 6. It is obvious that the power decreases with increasing cycle number, while the inner resistance increases continuously.

Fig. 7 shows the changing impedance spectra after every 100 cycles at SOC10 and 0 °C. With increasing cycle number, the impedance spectra show an increase of the cathode's charge-transfer resistance, which is in the frequency domain around 10<sup>0</sup>–10<sup>-1</sup> Hz. Between cycle number 400 to 500 the process decreases, which is due to a change in cell voltage (values are listed in Fig. 7). During the cells life the potential of the cathode increases significantly as shown in Fig. 10b marked by an arrow, which causes the change in cell voltage. Because the charge-transfer resistance of the cathode is very sensitive to voltage variation, as shown in Fig. 2, the process appears to be smaller and superposes the slightly risen process caused by aging as indicated by the arrows in Fig. 7a.

The resistance of the anode's charge-transfer process, located around 10<sup>1</sup> Hz, seems to decrease after the first hundred cycles and slightly increases in the following cycles, but to a much smaller extent than at the cathode.

The serial resistance increases continuously during cycling indicating a reduced ionic conductivity of the electrolyte and thus decomposition of the electrolyte during cycling or variation within the bulk material. The increase of the ohmic resistance by a factor 3 (Fig. 7) cannot only be explained by the decomposition of electrolyte. Considering diagrams of specific conductivity as a function of the amount of the conductive salt will support this theory. If the electrolyte's conductivity is reduced to one third the amount of the conductive salt should be reduced by a factor of 6, which is not realistic. Assuming that not only LiPF<sub>6</sub> decomposition takes place

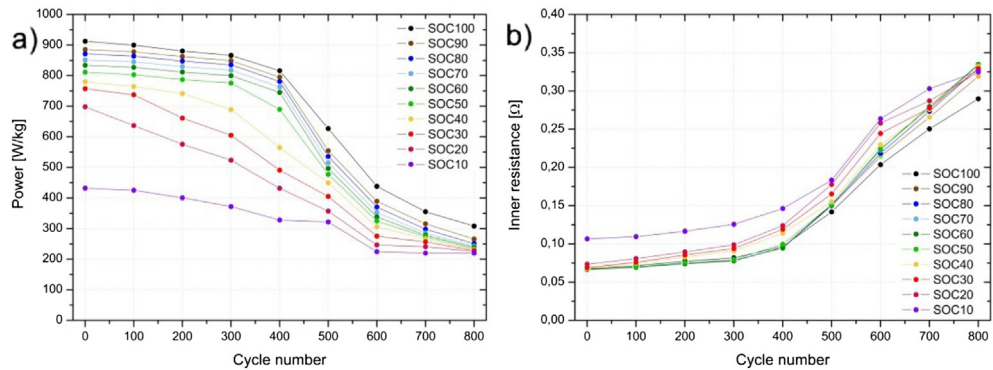


**Fig. 6.** a) Power and b) inner resistance evolution during cycling at room temperature for different SOCs. Together with the increase of the inner resistance the power decreases.

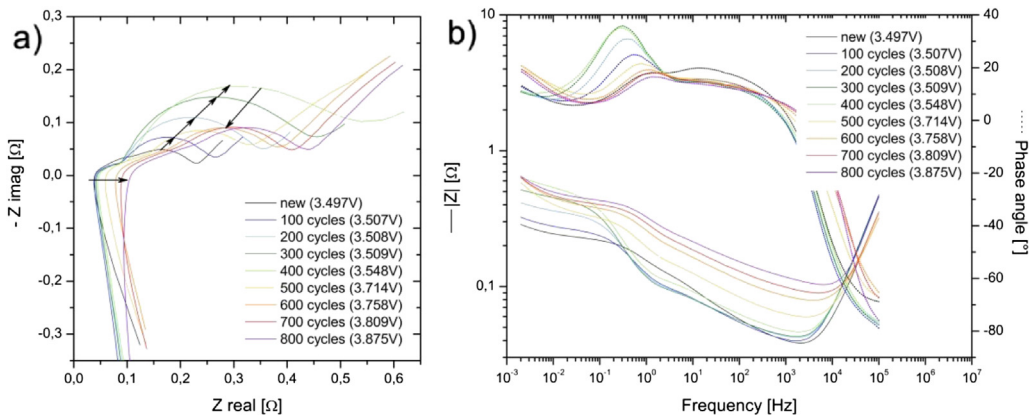


**Fig. 7.** Impedance spectra of cycle aged cell after every 100 cycles in a) Nyquist and b) Bode plots. All spectra are taken at SOC10 at 0 °C. The impedance increases from the initial state to 400–500 cycles due to aging and decreases then due to the change in cell voltage, which over-compensates the effect of aging.

but as well organic solvent decomposition leads to the fact that even more LiPF<sub>6</sub> has to be decomposed to diminish the electrolyte's conductivity by a factor 3. We propose the formation of an additional surface layer on the anode probably formed from decomposition products of the electrolyte, which is on top of the SEI, highly porous and soaked with electrolyte leading to a longer path way for the lithium ions to reach to the surface of the anode and thus an increase of the serial resistance. This layer is even growing into the pores of the separator, leading to an increased electrolyte resistance through the separator. This is supported by the fact that in aged cells separator and anode stick very well together and could not be separated very well. The presence of the layer will be shown later on in Figs. 11 and 12. This theory could explain the massive increase of the serial resistance as shown in Fig. 7.

### 3.4. Electrochemical investigation of the aged cell

Slow-sweep electrochemical analysis at a discharge rate of C/50 and additionally analysis at C/10 have been conducted at aged cathodes and anodes in order to determine the capacity loss caused by loss of active material (e.g. isolated particles or transition metal dissolution) or increase of inner resistance; slow discharge curves are plotted of anode and cathode to distinguish between these two effects. The following Table 1 gives an overview of the capacity of new and aged electrodes and the attributed mechanisms of capacity loss.

Discharge capacities at higher discharge rates may be highly influenced by large over-voltages and thus do not give information only about loss of active material. Very slow discharge rates (C/50)

**Table 1**

C/50 and C/10 capacities of new and aged electrodes, showing the capacity loss due to active material loss and due to increase of inner resistance (at C/10).

Electrode	C/50 Capacity [mAh cm <sup>-2</sup> ]		Capacity loss by active material loss [%]	∅ Capacity loss by active material loss [%]	C/10 Capacity [mAh cm <sup>-2</sup> ]		∅ C/10 Capacity loss [%]
	New	Aged			New	Aged	
Cathode	2.899	2.739	5.52	5.32	2.877	2.507	13.36
		2.740	5.49			2.486	
		2.750	5.14			2.484	
Anode	3.126	2.995	4.17	3.61	3.122	3.025	3.66
		3.065	1.97			3.005	
		3.026	3.18			2.993	

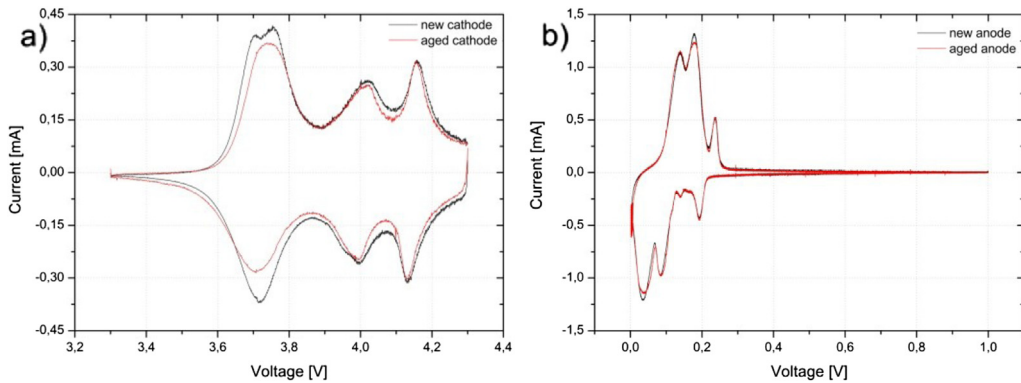


**Fig. 8.** Slow-scan cyclic voltammetry of new and aged cathode, scan-rate:  $5 \mu\text{V s}^{-1}$ . A decrease of the height of the NMC peak can be attributed to the loss of active material, while the height of the spinel peak stays the same.

minimize these over-voltages and allows us to estimate the capacity loss from active material loss, which is about 5.3% at the cathode and 3.6% at the anode. It can be seen that the new anode is oversized by 7% in capacity to ensure that all lithium from the cathode can be intercalated and lithium plating at the graphite surface is avoided.

Slow-scan cyclic voltammetry has been conducted at the aged anode and cathode (see Fig. 8). The aged anode shows marginal differences from the new anode in the cyclic voltammetry, thus indicating a retained initial capacity, while the aged cathode exhibits a reduced peak height, especially at the position of the NMC peak ( $\sim 3.7 \text{ V}$ ) [18] corresponding to loss of active material, which is in accordance to the already shown slow-sweep electrochemical analysis.

This means that the total cell capacity fade can be partially attributed to the loss of  $\text{Li}(\text{Ni}_{0.5}\text{Mn}_{0.3}\text{Co}_{0.2})\text{O}_2$  active material. Because the anode's capacity is over-dimensioned it is not expected to be a part of the total capacity fade.

Comparing the rate capability of new and aged anode and cathode shows that the cathode's rate capability drastically decreases, which can be seen in Fig. 9. The aged anode does not show large differences compared to the new cell.

Within this test only the discharge rates varied. The charging step was always conducted at a constant current rate of  $C/10$  and a 3 h constant voltage step at 4.3 V for the cathode and 5 mV for the anode, respectively. At the end of the test four additional cycles at  $C/10$  proved that no further aging was induced by this test. The initial capacity of the first four cycles was retained in the last four

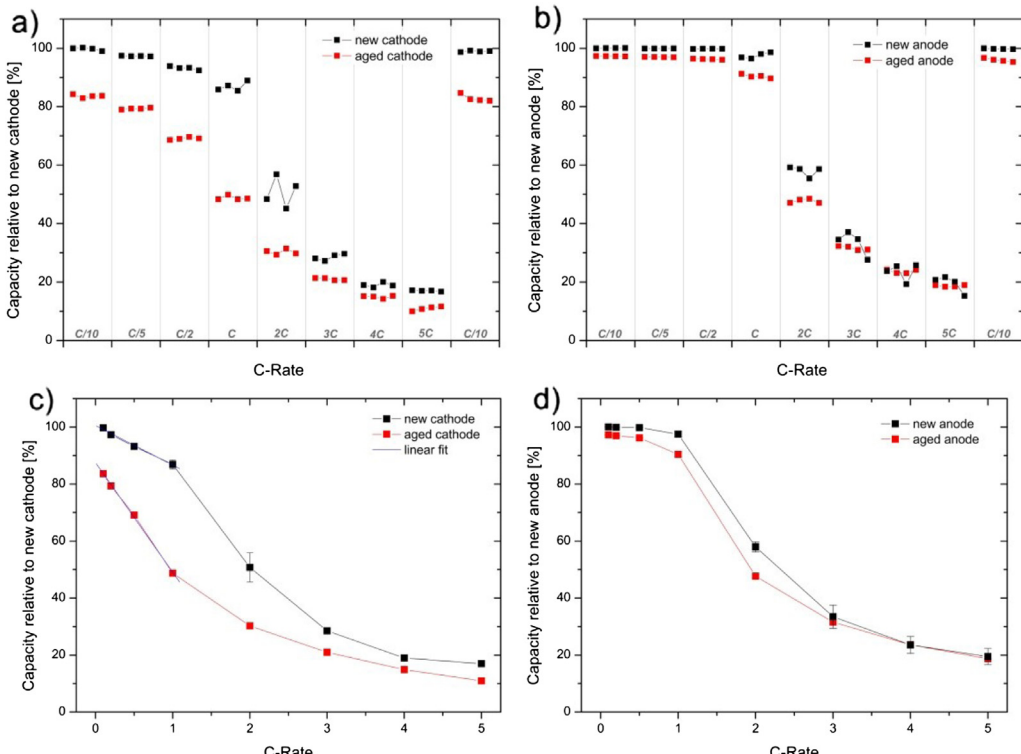


**Fig. 9.** Rate capability test of new and aged a) cathode and b) anode. The cathode shows a decreased rate capability while the anode only shows marginal differences. c) and d) give a different representation of a) and b) to clearly show two occurring mechanisms.

cycles in all tests. On closer examination of the aged cathode, it can be seen that significant changes in the discharge capacity are present even at small discharge rates. Even the new cathode suffers from drastic capacity fade at higher rates.

At higher rates (3C, 4C, 5C) the discharge capacities converge again. Fig. 9c and d gives a different representation of the data shown in Fig. 9a and b. Each data point in Fig. 9c and d represents the mean value and its corresponding standard deviation of four data points at each C-rate. It can be clearly seen that two different mechanisms are occurring in the cell. Data points representing C/10, C/5, C/2 and 1C have a linear correlation representing overall kinetics (charge transfer, diffusion, etc.) in the new and aged cell. The aged cathode shows a steeper decrease of the trend line compared to the new cell. The data points for higher C-rates ( $\geq 2C$ ) exhibit an exponential-like behaviour indicating that a second mechanism over-compensates the kinetic effects, seen at the small rates. This second mechanism may be caused by a depletion of lithium ions within the pores of the electrode. If too few lithium ions are transported to the surface of the electrode, a high over-voltage forms resulting in small discharge capacities. This mechanism may be reinforced by a limiting counter electrode. The current density of metallic lithium could be limiting for the cathode and could provoke the exponential-like behaviour of the curve. To find out the influence of the metallic lithium electrode, rate capability experiments with a different counter electrode should be performed. Comparing these data to those of the slow-scan electrochemical investigation (Table 1) and electrochemical impedance spectroscopy (see later) clearly shows the effect of an increased inner resistance. The 5.32% capacity loss at C/50 was assigned to loss of active material. At C/10 the capacity loss amounts to 13.36%. Assuming again the same amount of active material loss, this suggests that 8% of the capacity fade at C/10 is caused by an increased inner resistance. As the aged anode behaves unsuspiciously and the capacity loss at C/10 is nearly the same as at C/50, it is clear that the cathode is mainly responsible for the total increase of inner resistance of the 18650 cell.

In the experiment shown in Fig. 10a an EL-Cell with anode and cathode + metallic lithium reference electrode was charged with C/25 to 4.2 V, followed by a 3 h CV step at 4.2 V. With the help of the reference electrode the potential of anode and cathode was monitored during cycling. An EL-Cell with new electrodes (dashed lines) is compared to an EL-Cell made of aged electrodes (solid lines). The corresponding discharge step at a rate of C/25 is seen in Fig. 10b.

It is clear that the aged full cell has a greatly reduced capacity. The new and aged cathode potentials as well as the full cell voltages show differences. Due to a decreased capacity, the voltage level of

the aged cathode, and thus the aged full cell, changes significantly faster compared to the new cell. During charging (Fig. 10a) the voltage curves of the new and aged anode run at exactly the same potential. On closer examination it can be seen that the lower plateau of the aged graphite vs. lithium curve is not used to full capacity based on comparison to new graphite vs. lithium. As half of the graphite's capacity is stored at the lower plateau, this graph shows that nearly half of the graphite's capacity is unused in the cell's aged condition. Here the capacity is limited mainly by consumption of cycleable lithium in side reactions like surface layer growth, while only a small part is caused by loss of active material. Lithium is captured in the solid electrolyte interface at the surface of the anode and cannot be used to fully lithiate the cathode. Hence, the cathode is cycled at more positive potentials in the aged state compared to the new state which forces the anode to adopt a more positive potential in the discharged state (Fig. 10b). Transition metal dissolution at the cathode and incorporation into the SEI layer leads to partial damage of the layer and induces further growth of the SEI layer. In the present case the shift in anode and cathode potential is about 230 mV as marked in Fig. 10b).

### 3.5. Materials analysis of the aged cell

The surface of the electrodes has been investigated by SEM and EDS analysis. Comparing new and aged cathodes does not show large differences in their appearance. In contrast, the surface of the aged anode is rougher than the initial surface structure, meaning that the typical flake structure of graphite cannot be seen any more at the surface (see Fig. 11). We interpret this rough layer as the additional surface layer on top of the SEI layer, which causes the serial resistance to increase, as described before in the interpretation of the impedance spectra. At some positions the initial surface emerges beneath the surface layer as shown in the centre of Fig. 11b. During disassembling of the 18650 cell the separator has to be removed from the surface of the anode. In the aged state the separator can only be removed with increased effort. It is not clear if parts of this surface layer stick to the separator and are thus detached unintended.

EDS analysis proved that manganese is present at the aged anode's surface. Light microscopy images of cross-sections of aged electrodes showed that the aged cathode remained in its original state, but the anode slightly increased in thickness from 58  $\mu\text{m}$  (new) to 65  $\mu\text{m}$  (aged). Also the rough surface structure, marked in Fig. 11, can be seen as a thin layer of a few  $\mu\text{m}$  (Fig. 12b).

To see how the materials have changed during cycling, X-ray diffraction patterns were taken from new and aged anodes and cathodes. The electrodes were discharged at C/50 to SOC0 and

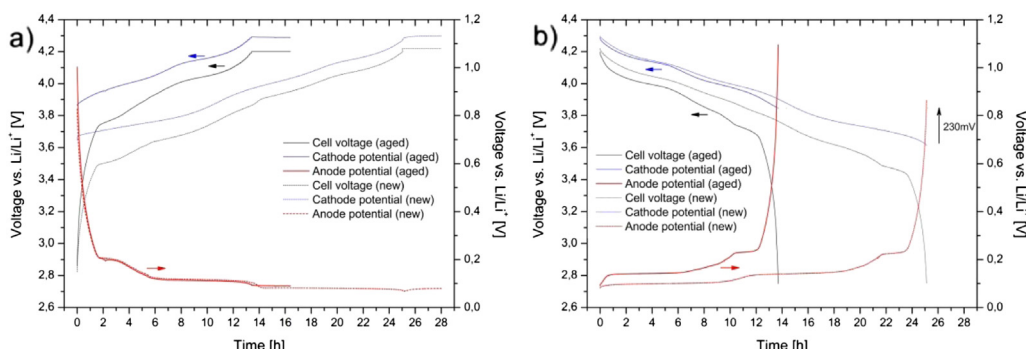


**Fig. 10.** Potential curves of a) charge and b) discharge of new (dashed line) and aged (solid line) full cell, black curve: cell voltage, blue curve: cathode potential, red curve: anode potential. The cathode limits the anode, which cannot be fully charged in the aged state. Main factor is the loss of cycleable lithium, which prevents the cathode from being fully charged. (For interpretation of the references to color in this figure legend, the reader is referred to the web version of this article.)

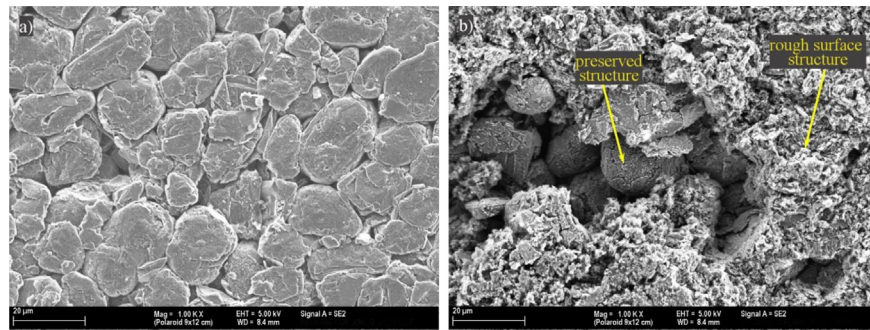


**Fig. 11.** SEM images of a) new and b) aged anode surface structure. Beneath the SEI layer the preserved graphite flake-like structure can be seen.

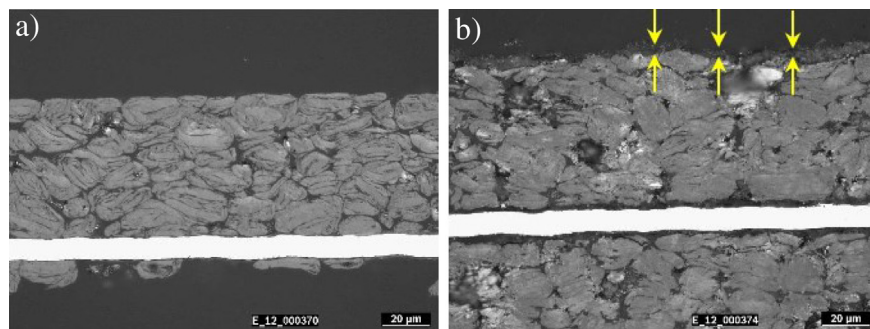


**Fig. 12.** Light microscopy images of polished cross-sections of a) new anode and b) aged anode. A few  $\mu\text{m}$  thick SEI layer can be found at the surface of the aged anode.

afterwards measured under argon atmosphere. The aged anode does not show differences in its peak pattern compared to the new cell, which is in accordance to Ramadass et al. [19]. No secondary phases could be detected at the aged cathode, but the pattern exhibits a decrease of the lattice volume of NMC whereas the lattice parameter of the spinel structure stays the same. Table 2 lists the lattice parameters of new and aged anodes and cathodes.

On closer examination of the individual lattice constants it can be seen, that parameter  $a$  tends to decrease slightly, while  $c$  increases significantly, corresponding to a decrease in interlayer distances and an increase of the distance between layers. The increase of parameter  $c$  can be attributed to a lower content of  $\text{Li}^+$  in the structure. Due to missing transition metals in the NMC material less  $\text{Li}^+$  can be stored between the layers leading to an increase of parameter  $c$  as one can see in the characteristic trend of Fig. 4b. Coming along with an increase of  $c$  a decrease of parameter  $a$  has to take place. This can be explained by a higher average oxidation number of Ni, Co and Mn ions. Because less  $\text{Li}^+$  can be intercalated into the structure the average oxidation number of the transition metals is higher than in the fully intercalated state, leading to a stronger interaction with the negatively charged oxygen ions and thus a decrease of the interlayer distance represented by parameter  $a$ .

Another method to prove loss of active material by transition metal dissolution is to analyze the aged anode by ICP-OES for

transition metals that have been transferred from the cathode. Transition metal dissolution was shown to be a relevant aging mechanism. The following Table 3 lists the detected transition metal concentrations of new and aged anode.

Dissolution of manganese can be caused by two main reaction mechanisms in the cell [20], which can be due to disproportionation of  $\text{Mn}^{3+}$  to  $\text{Mn}^{2+}$  and  $\text{Mn}^{4+}$  ions at low states of charge, or due to traces of HF within the electrolyte with  $\text{LiPF}_6$ . Because manganese ions do not change their oxidation state to  $\text{Mn}^{3+}$  during charging and discharging within the NMC, manganese dissolution caused by HF is more likely. Ni and Co do not show disproportionation reactions, which suggest the dissolution by HF to be presumable. Very often manganese dissolution is assigned to the  $\text{LiMn}_2\text{O}_4$  [20], but in this case no variation in the spinel lattice constant can be seen and Ni and Co dissolution takes place as well. Dissolved transition metals are transported through the electrolyte to the surface of the anode and incorporate into the SEI layer [3,4,20,21] leading to an increased SEI layer growth and loss of cycable lithium as shown in Fig. 10.

The aged electrolyte was analyzed by GC-MS analysis which clearly detected decomposition products from the solvent component ethylene carbonate. Electrolyte decomposition was already indicated by an increase serial resistance in the impedance spectra of Fig. 7 and could be also responsible for the formation of a porous cover layer on the anode surface.

Interestingly the anode performance is insignificantly influenced by the presence of transition metal atoms and an increased

**Table 2**

Lattice parameters of new and aged anodes and cathodes.

Electrode	$a$ Graphite [ $\text{\AA}$ ]	$c$ Graphite [ $\text{\AA}$ ]	$a$ Spinel [ $\text{\AA}$ ]	$a$ NMC [ $\text{\AA}$ ]	$c$ NMC [ $\text{\AA}$ ]
New anode	2.46(2)	6.71(2)	—	—	—
Aged anode	2.46(1)	6.71(4)	—	—	—
New cathode	—	—	8.21(8)	2.86(4)	14.26(3)
Aged cathode	—	—	8.21(5)	2.86(0)	14.27(8)

**Table 3**

Concentrations of transition metals in new and aged anode.

Electrode	Mn [ $\text{mg kg}^{-1}$ ]	Ni [ $\text{mg kg}^{-1}$ ]	Co [ $\text{mg kg}^{-1}$ ]
New anode	136	53	35
Aged anode	735	265	131

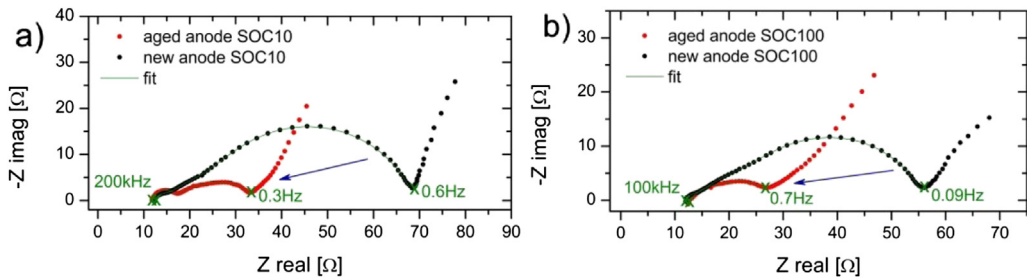


**Fig. 13.** Impedance spectra of new and aged symmetric anode at a) SOC10 and b) SOC100 in Nyquist plot. The overall impedance of the aged anode drastically decreases at SOC10 and SOC100 after aging. Additionally an increased particle-current collector contact resistance can be seen in the high frequency part.

SEI layer thickness, which can be seen in the rate capability test and the potential curves of Fig. 10. Although the influence on the rate capability test of a varied SEI layer after the preparation step is not clear.

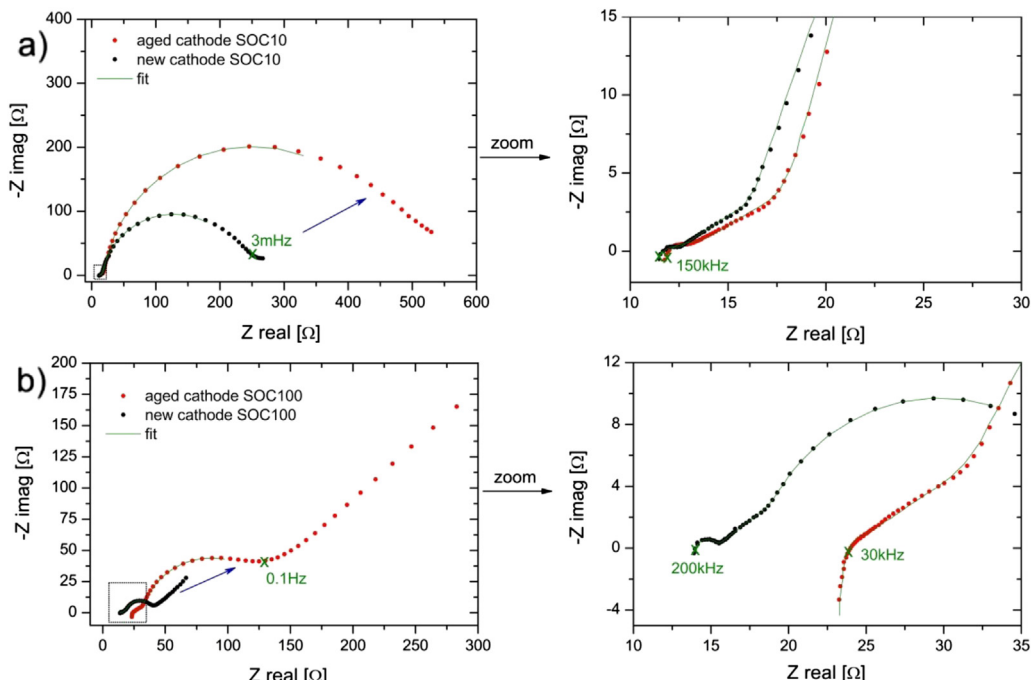
### 3.6. Investigation of the aged cell by impedance spectroscopy and DRT

Electrochemical impedance spectroscopy has been conducted on aged anodes and cathodes at defined potentials. As shown in Fig. 3 the new cell was characterized at various SOCs. Every SOC can be assigned to a defined potential. Aged anodes and cathodes were set and measured at these defined potentials, taken from the new electrodes, to eliminate the influence of the voltage dependence of impedance spectra. In the following graphs the curves are denominated with SOC10 and SOC100 which refers to the state of charge of the new cell. The Kramers–Kronig residuals are shown in Fig. S1 in the supporting information, representing the quality of the measured impedance spectra. The Kramers–Kronig residuals of all cells are below 0.4%, thus proving a very good data quality. For

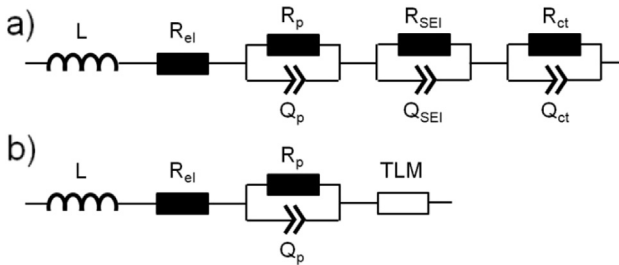
the aged and new cathode at SOC10 and 0 °C residuals higher as 1% could be observed. This can be attributed to a slightly time invariant behaviour affecting measured frequencies below 1 Hz. As the regarded frequency range for analysis is limited to lower frequencies, the measurements could be included in the analysis.

Fig. 13 shows the impedance spectra of new and aged anode at SOC10 and 100, as does Fig. 14 for the cathode.

In Fig. 13a and b it can be clearly seen that the charge-transfer resistance of the aged anode is reduced compared to the new one. This trend is present for SOC10 and SOC100. Particle-current collector contacts, predominantly appearing in the high-frequency domain of the impedance spectra significantly increased, which could be due to the difficulty described in Section 2.3, when the coating tends to flake off during reassembling the EL-Cells from half cells to symmetric cells. Understandably these increases in the high-frequency domain are not representative for an exclusive variation in particle-current collector contacts. Contrary to the anode, the aged cathode exhibits a remarkable increase of its overall resistance marked in Fig. 14a and b. Again SOC10 and SOC100 show the same trend.



**Fig. 14.** Impedance spectra of new and aged symmetric cathode at a) SOC10 and b) SOC100 in Nyquist plot. The overall impedance of the aged cathode increases at SOC10 and SOC100 after aging, indicating an increased charge-transfer resistance.



**Fig. 15.** Derived electrical equivalent circuit for new and aged a) anode and b) cathode at SOC10 and SOC100.

**Fig. S2 and S3** in the supporting information show the calculated DRT in order to derive an adequate electrical equivalent circuit to fit the shown impedance spectra. With this result of the DRT (3 appearing peaks) the corresponding electrical equivalent circuit is derived as shown in Fig. 15a.

The equivalent circuit for the anode consists of an inductor  $L$ , a resistor  $R$ , three  $RQ$ -elements.  $RQ$  elements are used instead of  $RC$  elements to describe the porous nature of the electrodes in the best way.  $L$  represents the inductivity from the measurement cables and  $R_{el}$  describes the ohmic resistance.  $RQ_p$  stand for the process appearing in the high-frequency range, which is probably a particle-current collector contact resistance [15]. The second  $RQ$  element describes processes from SEI layers, which are often partially overlapping with the following charge-transfer process. The third  $RQ$  models the charge-transfer process in the mid frequency domain. Constant phase elements are used to describe the porous electrode in the best way. As the observed frequency region does not comprise the diffusion, it can be discounted. The impedance spectra have been fitted in ZView and the obtained values are listed in Table 4.

The values show a reduction of the anode charge transfer resistance. The characteristic frequency for the anode charge transfer process stays the same in the new and aged state, indicating an unchanged material. The reduced charge transfer resistance can be explained by an increased graphite surface in the aged state. This assumption is maintained by the corresponding capacitances listed in Table 4. There it can be seen that the  $C_{ct}$  value of the new state is much smaller than of the aged state. Cracked or exfoliated particles might be the reason for this increased surface.

The second  $RQ$  element appearing at around 200 Hz, is attributed to the SEI layer at the surface [21] of the anode and shows a reduced resistance in the aged state. The decrease of the resistance of the SEI layer is very unexpected, because the presence of a highly distinctive SEI layer would suggest an increase in impedance. From the literature [4,20] it is well known that the SEI layer is growing during cycle aging, which is also confirmed from our results in Fig. 10, that shows loss of cycleable lithium due to continuous SEI-layer formation. But also results from the rate capability test showed that the anode's performance did not change significantly during aging, despite large amounts of transition metals found on

**Table 4**

Values of fitted impedance spectra from Fig. 14.  $R$  = resistance,  $C$  = capacitance,  $n$  = QPE-specific variable  $0.5 \leq n \leq 1$ .

Electrode	SOC	$R_p$ [ $\Omega$ ]	$R_{SEI}$ [ $\Omega$ ]	$C_{SEI}$ [F]	$n_{SEI}$	$R_{ct}$ [ $\Omega$ ]	$C_{ct}$ [F]	$n_{ct}$
Anode new	10	3.53	9.26	$9.61 \cdot 10^{-4}$	0.64	44.30	$1.52 \cdot 10^{-3}$	0.77
Anode aged	10	6.22	5.64	$1.37 \cdot 10^{-3}$	0.71	11.13	$6.70 \cdot 10^{-3}$	0.67
Anode new	100	3.36	9.07	$7.30 \cdot 10^{-4}$	0.67	32.61	$1.55 \cdot 10^{-3}$	0.75
Anode aged	100	6.41	5.45	$1.67 \cdot 10^{-3}$	0.69	10.74	$8.30 \cdot 10^{-3}$	0.67

**Table 5**  
Values of fitted impedance spectra from Fig. 15.

Electrode	SOC	$R_p$ [ $\Omega$ ]	$R_{ct}$ [ $\Omega$ ]	$\tau$ [s]	$n$	$L$
Cathode new	10	1.52	223.5	2.23	0.90	1
Cathode aged	10	3.02	464.5	4.76	0.91	1
Cathode new	100	1.78	22.75	0.25	0.89	1
Cathode aged	100	1.50	110.9	1.05	0.85	1

the surface. Out of the fitting data it can be seen that the resistance of the SEI layer decreases after aging, indicating a decreased SEI layer surface thickness, which could be explained by an unintended detachment of the layer during disassembling of the 18650 cell. The increasing  $n$  value indicates a smoother surface, which could be induced by the detachment. However the preparation step before measuring the impedance has also to be taken into account. The values have to be considered critically, because the SEI is definitely changed during removing of the electrodes from the 18650 cells, where the layer typically runs dry. Mechanical stress during preparation might also change the SEI layer. Because the curves of SOC10 and SOC100 are measured at two different cells small variations during the preparation (e.g. preparation time, hardness of mechanical stress) may have an influence on the shape of the SEI layer.

The third  $RQ$  element increased in case of the cell at SOC10 and reduced in case of the cell at SOC100. This  $RQ$  element, representing the particle-current collector processes is, as well as the SEI layer, highly influenced by the preparation. Delaminated regions already have strong impact on the appearance of the high-frequency process, which was the case in the aged anode at SOC10 (Fig. 13a).

With the help of the DRT (for more information see Supporting information) also the equivalent circuit for the cathode is derived (see Fig. 15b). In the Nyquist plot of Fig. 14a + b one very small and one dominant semicircle can be observed. These two semicircles are connected by a line at an angle of about  $45^\circ$  (see Fig. 14). The impedance spectrum with this shape can be described in its best way by the transmission line model (TLM) of Bisquert [22] for porous mixed phase electrodes. This thesis is supported by the DRT, where one main peak appears with its associated side peaks in the frequency region between 3000 Hz and 20 Hz, which is the characteristic pattern by the TLM (see Supporting information).

$L$ ,  $R_{el}$ , and  $RQ_p$  again describe the inductivity of the measurement cables, the ohmic resistance and particle-current collector contacts. The TLM represents charge transfers coupled with the electrolyte conductivity in the pores. The equivalent circuit model again did not consider the diffusion tail. With help of this equivalent circuit the impedance spectra of the cathode have been fitted in ZView and the obtained values are listed in Table 5. The fit values indicate an increased charge transfer resistance. The characteristic frequency decreased in both cases (SOC10 and SOC100) by about 1 order of magnitude.

Because the tortuosity and the electrochemical active surface are unknown, the length is fixed to 1 to achieve comparable values. It is assumed that geometries of new and aged cathode are comparable. The impedance increase of the aged symmetric cathode cell reveals that the increase in inner resistance of the 18650 cell is mainly caused by the cathode, which is in accordance to the data of the rate capability test.

#### 4. Conclusions

In this work the effect of continuous cycling on a battery's life time has been studied. Cycling was conducted on a commercial lithium ion battery containing  $\text{LiMn}_2\text{O}_4/\text{Li}(\text{Ni}_{0.5}\text{Co}_{0.2}\text{Mn}_{0.3})\text{O}_2$  as cathode and graphite as anode material.

The capacity fade during aging is mainly caused by loss of cycleable lithium, due to consumption of cycleable lithium for SEI growth. Transition metals from cathode dissolution have been found at the surface of the aged anode enhancing the SEI layer growth. It is well known, that SEI layer formation significantly increases when transition metals incorporate into the SEI [20]. To a minor extent also loss of active material at the cathode, mainly from  $\text{Li}(\text{Ni}_{0.5}\text{Co}_{0.2}\text{Mn}_{0.3})\text{O}_2$  is also responsible for the capacity fade of the cells. This could be either due to isolated particles within the electrode or also due to dissolution of transition metals from the cathode.

The increase of impedance and thus inner resistance of the cell is studied using EIS, both for the 18650 cells as well as for symmetric cells made from the electrodes of the 18650 cells. The rise of the cell resistance is mainly caused by an increase of the cathode's impedance. The EIS results clearly show an increase in the charge-transfer resistance of the cathode and an increase in the appropriate time constant.

Beside that, also the serial resistance of the cell increases by a factor of 3, which could be explained by electrolyte decomposition and the formation of a thick, porous film on the surface of the anode, that might also at least partially clog the pores of the separator.

An astonishing effect is the decrease of the anode's charge transfer resistance and the SEI layer resistance leading us to consider that the SEI layer may also be disturbed during the preparation step for the symmetric cells.

With the help of symmetric cells the impedance spectra of the 18650 cell during aging could be interpreted and the processes could be assigned to either the anode or the cathode. The DRT method proved to be a valuable tool to derive equivalent circuits for anode and cathode to fit the impedance spectra for new and aged cells.

These work clearly demonstrates that numerous electrochemical and analytical tools are necessary to fully understand the aging of lithium-ion batteries in detail. Nevertheless the deep understanding of aging mechanisms in lithium-ion batteries is a very important subject since it is essential for the use of these devices in automotive applications.

## Appendix A. Supplementary data

Supplementary data related to this article can be found at <http://dx.doi.org/10.1016/j.jpowsour.2013.11.080>.

## References

- [1] J. Belt, V. Utgikar, I. Bloom, *J. Power Sources* 196 (2011) 10213–10221.
- [2] M. Winter, J.O. Besenhard, M.E. Spahr, P. Novák, *Adv. Mater.* 10 (1998) 725–763.
- [3] P. Arora, R.E. White, M. Doyle, *J. Electrochem. Soc.* 145 (1998) 3647–3667.
- [4] M. Wohlfahrt-Mehrens, C. Vogler, J. Garche, *J. Power Sources* 127 (2004) 58–64.
- [5] M. Broussely, Ph. Biensan, F. Bonhomme, Ph. Blanchard, S. Herreyre, K. Nechev, R.J. Staniewicz, *J. Power Sources* 146 (2005) 90–96.
- [6] EL-Cell GmbH, [www.el-cell.com](http://www.el-cell.com).
- [7] C.H. Chen, J. Liu, K. Amine, *J. Power Sources* 96 (2001) 321–328.
- [8] H. Schichlein, A.C. Müller, M. Voigts, A. Krügel, E. Ivers-Tiffée, *J. Appl. Electrochem.* 32 (2002) 875–882.
- [9] A. Leonide, V. Sonn, A. Weber, E. Ivers-Tiffée, *J. Electrochem. Soc.* 155 (2008) B36–B41.
- [10] V. Sonn, A. Leonide, E. Ivers-Tiffée, *J. Electrochem. Soc.* 155 (2008) B675–B679.
- [11] T. Momma, M. Matsunaga, D. Mukoyama, T. Osaka, *J. Power Sources* 216 (2012) 304–307.
- [12] J.P. Schmidt, T. Chrobak, M. Ender, J. Illig, D. Klotz, E. Ivers-Tiffée, *J. Power Sources* 196 (2011) 5342–5348.
- [13] D. Aurbach, M.D. Levi, E. Levi, H. Teller, B. Markovsky, G. Salitra, U. Heider, L. Heider, *J. Electrochem. Soc.* 145 (1998) 3024–3034.
- [14] A. Funabiki, M. Inaba, Z. Ogumi, S.-I. Yuasa, J. Otsuka, A. Tasaka, *J. Electrochem. Soc.* 145 (1998) 172–178.
- [15] J. Illig, M. Ender, T. Chrobak, J.P. Schmidt, D. Klotz, E. Ivers-Tiffée, *J. Electrochem. Soc.* 159 (2012) A952–A960.
- [16] G. Amatucci, A. Du Pasquier, A. Blyr, T. Zheng, J.-M. Tarascon, *Electrochim. Acta* 45 (1999) 255–271.
- [17] K.-W. Nam, W.-S. Yoon, H. Shin, K.Y. Chung, S. Choi, X.-Q. Yang, *J. Power Sources* 192 (2009) 652–659.
- [18] N. Yabucchi, Y. Makimura, T. Ohzuku, *J. Electrochem. Soc.* 154 (2007) A314–A321.
- [19] P. Ramadass, B. Haran, R. White, B.N. Popov, *J. Power Sources* 112 (2002) 614–620.
- [20] J. Vetter, P. Novák, M.R. Wagner, C. Veit, K.-C. Möller, J.O. Besenhard, M. Winter, M. Wohlfahrt-Mehrens, C. Vogler, A. Hammouche, *J. Power Sources* 147 (2005) 269–281.
- [21] P. Ramadass, A. Durairajan, B. Haran, R. White, B. Popov, *J. Electrochem. Soc.* 149 (2002) A54–A60.
- [22] J. Bisquert, G. Garcia-Belmonte, F. Fabregat-Santiago, A. Compte, *Electrochim. Commun.* 1 (1999) 429–435.